The effect of copper doping in α-MnO2 as cathode material for aqueous Zinc-ion batteries

Lan, R., Gkanas, E., Sahib, A. J. S., Greszta, A., Bhagat, R. & Roberts, A

DOI 10.1016/j.jallcom.2024.174528
ISSN 0925-8388
ESSN 1873-4669

Publisher: Elsevier

Journal of Alloys and Compounds 992 (2024) 174528

Contents lists available at ScienceDirect

Journal of Alloys and Compounds

journal homepage: www.elsevier.com/locate/jalcom

The effect of copper doping in α-MnO_2 as cathode material for aqueous Zinc-ion batteries

Rong Lan *, Evangelos Gkanas, Ali Jawad Sahib Sahib, Agata Greszta, Rohit Bhagat, Alexander Roberts

Centre for E-Mobility and Clean Growth, Coventry University, Coventry CV1 2TL, United Kingdom

ARTICLE INFO

Keywords:
Manganese Dioxide
Copper Doping
Cathode Materials
Zinc-ion Batteries

ABSTRACT

Copper-doped Manganese Dioxide has been synthesised through a simple hydrothermal method at different doping levels. The synthesised materials have been characterized by X-ray diffraction (XRD), and scanning electron microscopy (SEM) to determine the composition, structure, and morphology. All the Cu doped MnO_2 are found to be single phased. Their electrochemical properties as cathode for Zinc-ion batteries are studied by cyclic voltammetry (CV), galvano-static charge / discharge (GCD) and electrochemical impedance spectroscopy (EIS), using 3 M $ZnSO_4$ + 0.3 $MnSO_4$ solution as the electrolyte. 3.8% Cu doped MnO_2 has shown the highest initial capacity of 379.5 mAh g^{-1} at 0.02 A·g^{-1}, and 304.4 mA h g^{-1} at 0.5 A g^{-1}, but experienced fast fading with a poor capacity retention of 56.8% after 100 cycles. 7.4% Cu doping gives lower capacity, while 5.9% doping shows a higher discharging capacity (320.0 mAh·g^{-1} at 0.02 A·g^{-1} and 269.3 mAh·g^{-1} at 0.5 A·g^{-1}) and improved stability (85.8% capacity retention after 100 cycles), better than non-doped MnO_2 electrode (284.4 mAh g^{-1} at 0.02 A g^{-1} and 252.1 mAh·g^{-1} at 0.5 A g^{-1}, capacity retention 76.7%). The samples show satisfactory capacity and rate capability while the cycling stability is not ideal, which may relate to the needle like morphology and nanoscale particle size. CV tests revealed that the electrochemical process is mainly diffusion controlled. The zinc ion diffusion coefficient is tested to be in the range of 10^{-12} cm^2·s^{-1} from both CV and EIS tests and showed the same trend in their electrochemical capacity. Doping of Copper in MnO_2 reduced the polarization on electrode, improved the electrochemical reversibility, as evidenced by the reduction of the redox peak potential difference from 0.31 to 0.24 V at 1.1 mV·s^{-1}, and from 0.45 V to 0.31 V at 5 mV·s^{-1}. Whilst the cell resistance of non-doped MnO_2 increased from 1.78 Ω to 7.39 Ω after cycling, the cell resistances of all Cu-doped cathodes reduced, indicating improved electronic conductivities after cycling. These results indicate that Cu-doping is effective to increase the conductivity of the materials, reduce the polarization during charge and discharge, and improve the cycling stability of MnO_2 cathode.

1. Introduction

Aqueous batteries, or water-based batteries, offer several benefits compared to traditional non-aqueous (organic electrolyte) batteries, especially in safety, environmental benignity, and cost-effectiveness [1–3]. Among them, aqueous Zinc-ion batteries (ZIBs) are the most investigated [4–6]. ZIBs are promising for large-scale energy storage applications [1–4] e.g. grid-level energy storage systems, because their manufacturing processes are relatively simple with less constraints, and the materials used are widely available. While zinc-ion batteries have several advantages, they also face significant challenges to be addressed before their commercial implementation. Current ZIBs have a shorter cycle life compared to other battery technologies with the repeated insertion and extraction of zinc ions during charging and discharging cycles causing the electrodes to undergo structural changes and degrade over time, limiting the number of cycles the battery can withstand. ZIBs typically operate at a lower voltage compared to other battery chemistries which limits their application in devices or systems that require higher voltage levels. While ZIBs can offer high energy density compared to other aqueous batteries, they generally have lower energy density compared to lithium-ion batteries (LIBs). ZIBs have slower kinetics, leading to limited charge/discharge rates and lower power capabilities. [7]

Improvement in electrode materials (both anode [8–10] and cathode

* Corresponding author.
E-mail address: rong.lan@coventry.ac.uk (R. Lan).

https://doi.org/10.1016/j.jallcom.2024.174528
Received 4 December 2023; Received in revised form 10 April 2024; Accepted 15 April 2024
Available online 19 April 2024

[6,11–15]), electrolyte formulation [5,16–20] interface regulation and battery designs [21–23] are the key to addressing these limitations. Manganese dioxide (MnO_2) is the most commonly used cathode material in ZIBs [24–28], with some favourable characteristics [29], but challenges remain including: (1) Low conductivity: MnO_2 is inherently a poor electronic conductor, resulting in higher internal resistance, lower power output, and reduced columbic efficiency. (2) Large volume expansion: MnO_2 experiences significant volume expansion and contraction during charging and discharging, leading to mechanical stress with cracking and self-pulverisation resulting ion loss of cycle life. (3) Irreversible side reactions: MnO_2-based cathodes can experience irreversible reactions during cycling, resulting in a reduced reversible capacity and overall energy storage capability of the cell. (4) Formation of surface layers: the formation of insulating layers on the surface of the cathode material can occur during cycling, hampering the ion diffusion and electron transport. [30] (5) Limited voltage range: MnO_2-based cathodes typically operate within a limited voltage range, which can restrict the energy storage capacity and application range of the battery, not suitable for high-voltage applications where higher energy densities are required. Strategies have been proposed to solve above problems [31], such as atomic engineering [32], nano-structuring the MnO_2 material[33], incorporating conductive additives[34], and optimizing electrolyte composition[35] to enhance the conductivity, stability, and cycling performance of the cathode. These efforts aim to improve the overall performance and viability of MnO_2-based ZIBs for various applications.[36]

Since 2021, doped MnO_2 has been an area of active research and development in the field of energy storage. Various dopants, including transition metals (e.g., Fe, Co, Ni) [37–43], non-metals (e.g., N, F, S) [44–50], and carbon-based materials [51,52], have been studied for doping MnO_2. Doping can enhance the electron transport, mitigate the low conductivity issue associated with pure MnO_2, and improve the cycling stability [45,46,53,54]. It can also reduce the volume expansion and contraction of MnO_2 during cycling, mitigating the mechanical stress and strain that lead to material degradation [45,46,48]. Doping strategies have been investigated to expand the voltage range of MnO_2-based cathodes. By incorporating specific dopants, researchers aim to extend the operating voltage of MnO_2 beyond its intrinsic limit. This expansion can enable higher energy densities and make doped MnO_2 suitable for applications requiring increased voltage levels. The choice of dopant and doping method depends on the desired improvements in conductivity, stability, and electrochemical performance. Doping methods include chemical synthesis routes [30,49], electrochemical deposition[55–58], and chemical / physical vapour deposition techniques[59,60]. The development and optimization of doped MnO_2 cathodes in energy storage applications are ongoing, with new research findings and progresses continually emerging.

Copper-doped MnO_2 refers to the incorporation of copper ions (Cu^{2+}) into the crystal structure of MnO_2 [61]. This doping process involves substituting some of the Mn atoms with Cu atoms, altering the composition and properties of MnO_2. Copper doping in MnO_2 can increase the overall conductivity by facilitating charge transport within the crystal lattice. Copper doping has the potential to enhance the electrochemical performance of MnO_2, including the reversible capacity, cycling stability, and rate capability, making it more suitable for energy storage applications. Doping with copper ions can influence the structural stability of MnO_2 by mitigating the volume expansion and contraction issues, improving the cycling stability and prolonging the material's lifespan. The extent of copper doping in MnO_2 can vary depending on the desired properties and specific applications. The doping level needs to be carefully controlled to balance the conductivity enhancement and maintain the structural integrity of the material.

Copper-doped MnO_2 can be synthesized through various methods, such as solid-state reaction, hydrothermal synthesis, or sol-gel methods. The choice of synthesis method affects the homogeneity, purity, and overall properties of the doped material. Copper-doped MnO_2 has potential applications in various electrochemical devices including fuel cells [62,63] and metal air batteries [64,65], including lithium-ion batteries [61,66–68], Zinc-ion batteries [38,69–74], supercapacitors [75–78], and hybrid capacitors. It is also explored for catalytic and electrochemical sensing applications due to its modified properties [79–83]. Cu doped MnO_2 through a wet-chemical method was studied as the potential cathode materials for Lithium-ion batteries. [61] The doping effect was investigated on the improvement for the magnetic and electrical properties. Cu−intercalated δ−MnO_2 was obtained through an ion exchange treatment by immersing δ−MnO_2 powders in $CuSO_4$ solution, with MnO_2 synthesised through hydrothermal reaction[69]. Copper doping at different levels is not studied. Binder-free Cu-doped ε-MnO_2 has been synthesized through electrodeposition, when copper is co-deposited with MnO_2. [56] The best performance from this research came from the sample deposited on Carbon Nano Tube (CNT) film. Sputtered Cu on MnO_2 also showed a good performance in Zinc-ion batteries. From these previous research, Copper doped MnO_2 is a promising cathode for Zinc-ion batteries.

Different doping levels, synthesis techniques, and characterizing the performance of copper doped MnO_2 in battery systems and other energy storage applications still need to be investigated. In this paper, copper doped MnO_2 was synthesised through a simple hydrothermal process, and was investigated as the cathode material for ZIB, aiming to optimize the doping level for better properties and performance of MnO_2 for practical and efficient use in aqueous ZIBs.

2. Experiments

2.1. Materials

$KMnO_4$ (99%, Thermo Scientific Chemicals), $MnSO_4$ (99+%, Thermo Scientific Chemicals), $CuSO_4$ (>99.0%, Acros Organics, UK), 1-Methyl-2-pyrrolidinone (NMP, 99+%, Thermo Scientific Chemicals) Zinc foil (99.98%, thickness 1 mm, Alfa Aesar), glass fibre (GF6, Whatman), are purchased from Fisher Scientific, UK. Poly (vinylidene fluoride) (PVDF), and carbon black were purchased from GELON LIB GROUP, China.

2.2. Preparation of MnO_2

0.227 g $MnSO_4$ were dissolved in a beaker containing 10 ml deionised (DI) water under magnetic stirring for 10 minutes at 400 rpm. Calculated amount of $CuSO_4$ according to the molar ration to the final MnO_2 at 10%, 20%, and 30% was added and was kept stirring until fully dissolved. 10 ml $KMnO_4$ (0.1 M) was added to the above solutions slowly under stirring. The mixture was kept in ultrasonic bath for 0.5 h before being moved to an autoclave with a 30 ml Teflon liner, then reacted at 120 ℃ for 12 hours. After cooling the product to room temperature, it was then centrifugally washed with deionized water, and dried under vacuum at 60 ℃ for 12 hours. The collected powder was then calcined at 400 ℃ for 2 hours. The obtained samples are referred to as MC0 for non-doped MnO_2, and MC1 MC2 and MC3 for Cu doped MnO_2 from low to high doping level, individually.

2.3. Characterization

2.3.1. Morphology and chemical phase analysis

X-ray diffraction (XRD) tests were performed on a Bruker D8 Advance Diffractometer in Bragg-Brentano geometry with Cu Kα radiation λ = 1.5404 Å and a diffracted beam graphite monochromator. Powder X ray diffraction data is recorded for the 2θ angle range between 20° and 90° at room temperature with step size 0.0495° at 15 s per step. The observed XRD data is indexed with powder X software[84] and then subjected to Rietveld refinement with GSAS II [85]. Morphology and elemental composition of the materials were characterised using scanning electron microscopy (SEM) (1530 VP Field Emission Gun Scanning Electron Microscope (FEG-SEM), Carl Zeiss, Germany) and energy

dispersive X-ray spectroscopy (EDS) (X-MAX EDX, Oxford Instruments, UK).

2.3.2. Electrochemical analysis

The electrochemical performances of MC0, MC1, MC2, MC3 cathodes for aqueous ZIBs were investigated in CR2032 coin cells. The as-prepared MnO_2 samples were used as electrode active material. They were mixed with carbon black and poly (vinylidene difluoride) in an 8:1:1 wt ratio and dispersed in N−methyl−2−pyrrolidone solvent. The obtained ink was transferred onto stainless steel mesh substrate and then dried at 80 °C for 10 hours. The casted electrode was then cut into disks of a diameter of 1.6 mm, with a final mass loading of 1.4 1.5 mg cm^{-2}. CR2032 coin cells are assembled using the as prepared MnO2 cathode, polished zinc foil anode (99.98%, thickness 1 mm, Alfa Aesar), glass fibre as separators (GF6, Whatman), and 3 M $ZnSO_4$ + 0.3 M $MnSO_4$ solution as electrolyte.

Electrochemical performances of the as-assembled CR2032 full cells were assessed through Electrochemical Impedance Spectroscopy (EIS), Cyclic Voltammetry (CV), and Galvanostatic Charge / Discharge (GCD) cycling using a VMP3 multi-potentiostat (Bio-Logic Science Instruments SAS, France, EC-Lab software). All the electrochemical performance was tested at 25 ℃. The voltage window of GCD and CV tests were 1–1.8 V. CV scanning tests were carried out at 0.1–5 mV s^{-1}, respectively, with GCD at current densities between 0.02 and 0.5 A g^{-1}, and EIS at a frequency range from 10^{-2} to 10^{6} Hz, at a perturbation amplitude of 10 mV.

3. Results and discussions

3.1. SEM tests of the non-doped and copper doped MnO_2

Fig. 1 shows the morphology of the synthesised MnO_2 materials from scanning electron microscopy (SEM), presenting needle-like primary particles with width of 20–50 nm and length of 400–800 nm. The size of the nano-needles seems to be reducing slightly with the doping of copper increases. Energy dispersive X-ray spectroscopy (EDS) analysis shows

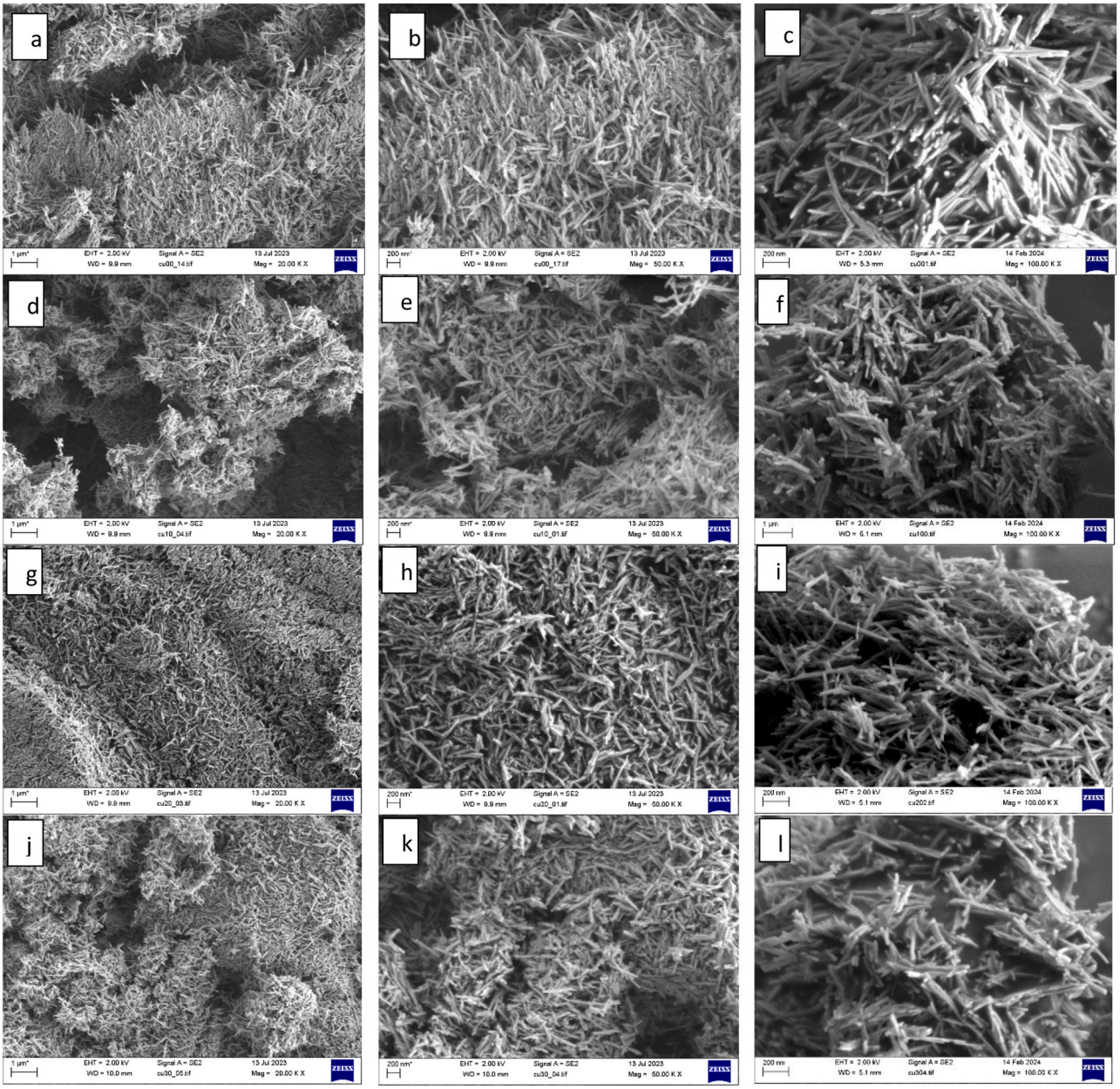

Fig. 1. SEM image of the synthesised MnO_2 at different copper doping: a), b), c) MC0; d), e), f) MC1; g), h), i) MC2; j), k), l) MC3.

even distribution of the elements and indicates that the copper doping level is significantly lower than expected, which turns out to be 3.82% of Cu for MC1, 5.89% of Cu for MC2 and 7.43% of Cu for MC3, in molar percentage.

3.2. XRD characterisation of the cathode materials

Powder X-Ray diffraction was used to examine the phase and crystallinity of the prepared samples. All samples exhibit identical sharp diffraction peaks, which can be indexed to the pure tetragonal phase of α-MnO_2 (JCPDS No. 00–44–0141.), space group I4/m. The XRD results indicate that all the samples are single phase as shown in Fig. 2, which has been further confirmed by retrieved refinement. The refined XRD pattern is shown in Fig. 3.

The refined lattice constants are listed in Table 1 and shown in Figure S1. As compared with the reported lattice parameters of α-MnO_2, a = b = 0.9785 nm and c = 0.2863 nm (ICSD: 44–141), in general the lattice parameters a / b increased with increasing level of copper doping. While c decreased slightly in MC1, it increased in MC2 and MC3. Since the valance state of Cu is lower than Mn, doping of copper will introduce oxygen vacancies into the lattice, which causes the lattice constant to reduce slightly. With higher doping, the oxygen vacancies increase, and the metal – oxygen bonding become weaker, which leads to the increase of the lattice constants. The lattice expansion due to doping indicates loosened lattice constraints in the nanostructures.

The particle size of the samples was also calculated from Sherrer's equation [86,87].

$$D = \frac{K \times \lambda}{\beta \cos\theta} \tag{1}$$

Where D is the particle size, K is a dimensionless shape factor, here we use K = 0.9. λ is the wavelength of CuKα1, which is 1.5406 Å. β is the line broadening at half the maximum intensity (FWHM), after subtracting the instrumental line broadening, in radians. θ is the Bragg angle. The particle size listed in Table 1 is based on the data at the strongest (211) peak at 2θ ≈ 37.5°. The calculated particle size is in the range of 80–110 nm, which is fairly closed to the value observed by SEM (Fig. 1).

The theoretical density is calculated using the following equation,

$$\rho = \frac{1.66 \times Z \times MW}{V} \tag{2}$$

Where ρ is the theoretical density, Z is the number of molecules in each unit cell, MW is the molecular weight in g mol^{-1}, V is the lattice volume

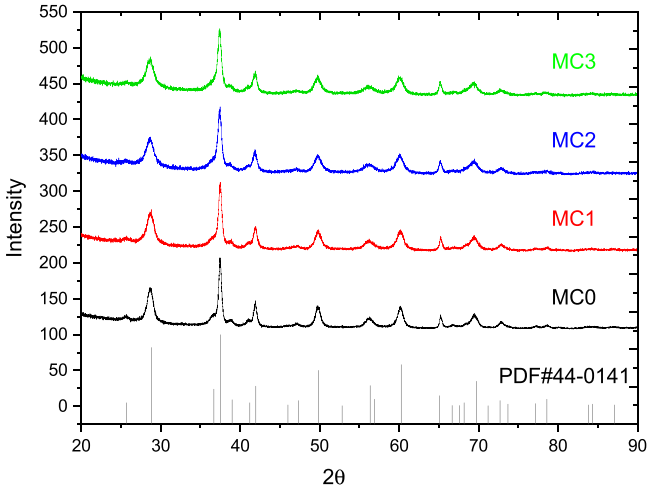

Fig. 2. XRD patterns of the synthesised MnO_2 samples with different level of copper doping.

in $Å^3$. For α-MnO2 with spece group I4/m (87), Z = 8. The calculated theoretical density of the four samples are listed in Table 1. With the increased doping level of copper, the theoretical density gradually increases from sample MC0 to MC3.

The surface area was calculated using the following equation,[86, 88–92]

$$S = \frac{6000}{D \times \rho} \tag{3}$$

Where S is the surface area, m^2/g, D is the particle size, ρ is the theoretical density. The calculated surface area for the four samples are also listed in Table 1. The copper doped samples have slightly higher surface area than undoped MnO_2.

The crystallinity percentage of the samples is calculated by the following equation[86].

$$\%Crystallinity = \frac{A_{cp}}{A_{ta}} \times 100 \tag{4}$$

Here, Acp is the area under crystalline peaks, Ata is the total area of the XRD peaks.

3.3. Cyclic Voltammetry tests of the zinc-ion batteries

To investigate the kinetics, cyclic voltammetry (CV) method [93] was applied at different sweep rates of 0.1–5 mV/s with a voltage range of 1.0–1.8 V versus Zn^{2+}/Zn in assembled CR2032 coin cells. Fig. 4 shows the CV tests before and after the cell cycling. Fig. 4a) shows the CV tests at 0.1 mV/s. In the reduction scan from 1.8 V to 0.8 V, two peaks appear at around 1.4 V and 1.3 V vs. Zn/Zn^{2+}, which can be attributed to Zn^{2+} or H^+ ions insertion into the MnO_2 host structure. [94] The oxidation scan towards 1.8 V also presented a peak at approximately 1.55 V vs. Zn / Zn^{2+}, corresponding to the oxidation of Mn^{3+} back to Mn^{4+} and the de-insertion of Zn^{2+} ions. The CVs at a scan rate of 0.1 mV s^{-1} appeared to be stable and consistent. CV curves are well overlapped, indicating good reversibility of cathode, except for the slight reduction of the peak current at 1.3 V, which reveals a decreased contribution to the capacity from H^+ ions. This could be caused by the high pH value of the electrolyte that limited the supply of H^+ ions. In the cathodic/anodic scans, the redox peaks appeared at the same location for all the cathodes, evidencing that Cu doped cathodes possess similar redox reactions to MnO_2 cathode, and does not significantly affect the electrochemical process or storage mechanism of MnO_2.[21]

The CV results at 0.1 mV of the samples showed that doping reduced the redox peak potential differences. With copper doping, the oxidation peaks shifted to the left while the reduction peaks shifted to the right, which brings down the redox peak potential difference from 0.19 to 0.16 V at 0.1 mV·s^{-1} scanning speed, from 0.29 V to 0.26 V at 1.1 mV·s^{-1} scanning speed, and from 0.41 V to 0.30 V at 5 mV·s^{-1} scanning speed (Fig. 5). After cycling, the reduction in redox peak potential difference became more significant. As shown in Fig. 5, the peak potential difference is smaller at low scan rate and became even bigger at higher scanning rate, compared to the trend of the results from the fresh cells. It comes down from 0.20 V to 0.18 V at 0.1 mV·s^{-1} scanning speed, from 0.31 V to 0.23 V at 1.1 mV·s^{-1} scanning speed, and from 0.45 V to 0.30 V at 5 mV·s^{-1} scanning speed. All the copper doped samples showed similar reduction in the redox peak potential difference despite that their doping levels are different. After cycling, the redox peak potential difference for MC0 (non-doped) increased from 0.19 V to 0.20 V at 0.1 mV·s^{-1}, from 0.29 V to 0.31 V at 1.1 mV·s^{-1}, and from 0.41 V to 0.45 V at 5 mV·s^{-1}; whilst for the doped samples, the redox peak potential difference increased from 0.16 V to 0.18 V only at 0.1 mV·s^{-1}, but reduced from 0.26 V to 0.23 V at 1.1 mV·s^{-1}, and from 0.45 V to 0.41 V at 5 mV·s^{-1}, after cycling. These results indicate that copper doping has effectively reduced the polarization on the electrode.

A dominating pair of redox peaks exhibits increasing currents when

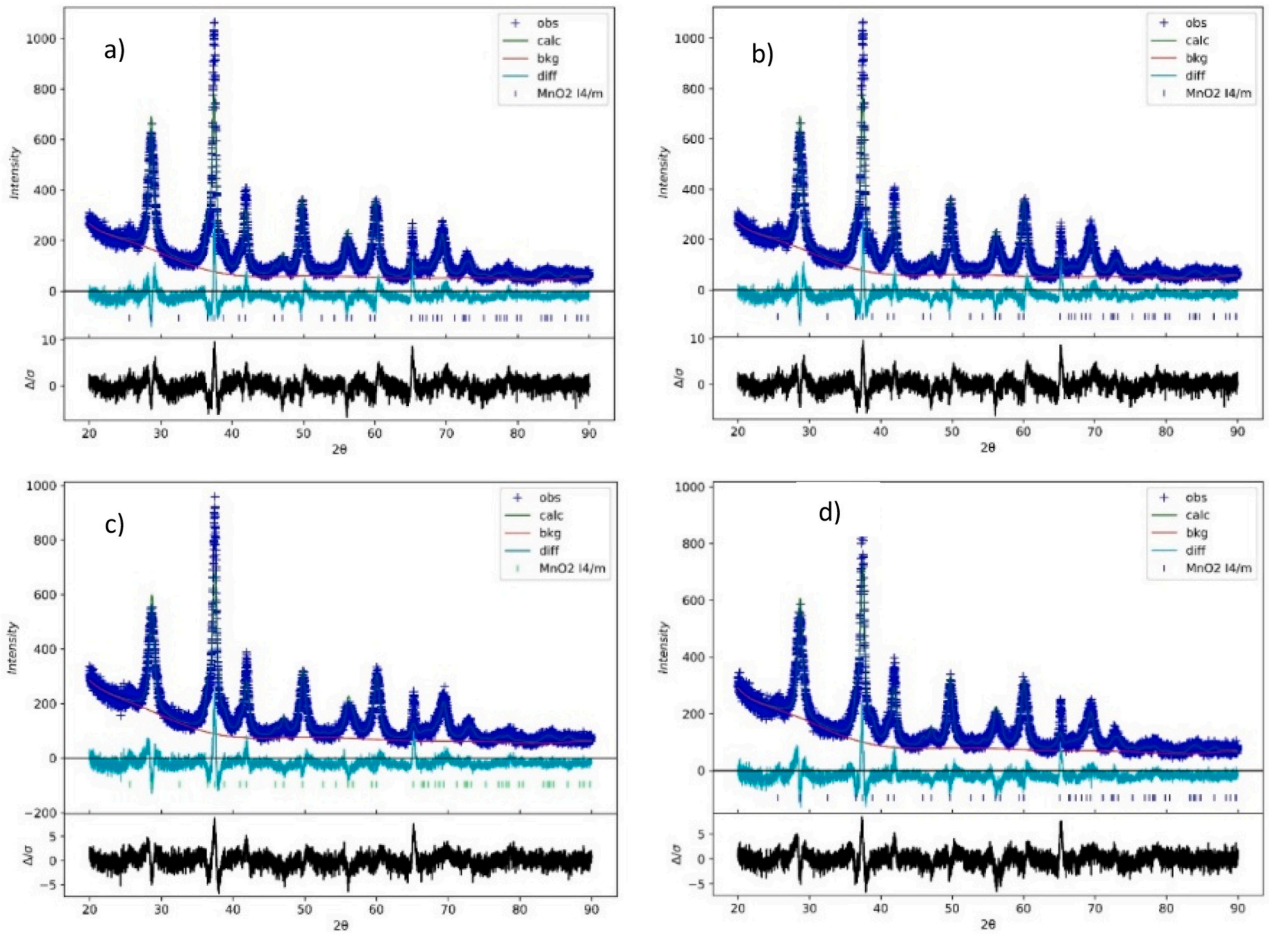

Fig. 3. XRD Rietveld refinement (GSAS II) patterns of the non-doped and copper doped MnO_2 samples: a) MC0; b) MC1; c) MC2; d) MC3.

Table 1
Key crystallographic parameters and grain properties of the samples.

Sample	Composition	Lattice parameters			Particle size (nm)	Theoretical density (g cm^{-3})	Sur-face area (m^2/g)	Crystallinity (%)
		a (Å)	C (Å)	V (Å^3)				
MC0	MnO_2	9.8232(3)	2.8624(5)	276.21(5)	111.06(2)	4.1798(4)	12.92(4)	88.1
MC1	$Mn_{0.962}Cu_{0.038}O_{2-\delta}$	9.8310(4)	2.8647(2)	276.87(3)	86.89(8)	4.1855(1)	16.49(6)	83.3
MC2	$Mn_{0.941}Cu_{0.059}O_{2-\delta}$	9.8330(2)	2.8642(9)	276.94(3)	79.17(7)	4.1931(1)	18.07(2)	84.0
MC3	$Mn_{0.926}Cu_{0.074}O_{2-\delta}$	9.8338(8)	2.8653(8)	277.09(7)	81.23(7)	4.1969(7)	17.59(7)	86.3

the sweep rates increase. The electrodes do not present a capacitive behaviour of the electrode. The capacitive effect is characterized by analysing the cyclic voltammetry data at different sweep rates as in Eq. (5) [93]:

$$i = av^b \tag{5}$$

In which i is the specific peak current, ν is the potential sweep rate, and a, b are parameters that can be fitted from the experimental data. Eq. (1) can be taken with logarithm and can be expressed according to Eq. (2):

$$lni = lna + blnv \tag{6}$$

The b value is the slope of the linear fitting of lni versus lnν. When b value is close to 1, the system is mainly capacitance controlled; when b value is close to 0.5, the Zn^{2+} ion insertion process dominates with the redox reaction limited by the diffusion-controlled behaviour. Figure S5 shows the ln i versus ln ν plots at oxidation and reduction process of the cyclic voltammogram.

The bo (oxidation process) and br-$_{Zn}$ (reduction process of Zn^{2+} peak) br-$_H$ (reduction process with H^+ de-escalation) of the cathodes, obtained from the above fitting (plotted in Figure S5) are listed in the Table 2.

The average b values are close to 0.5, which implies that the redox reactions on cathodes are controlled by the diffusion process. MnO_2 is a transition metal oxide that typically displays the pseudo-capacitance behaviour [95]. The capacitive-controlled process occurs only on the surface. However, our MnO_2 samples turned out to be mainly diffusion-controlled processes. This means, the insertion/extraction of ions occur not only on the surface but also the bulk. The result suggested a fast Zn^{2+} ion insertion/extraction or high-rate property for the battery.

When the process is diffusion controlled, the diffusion coefficient can be estimated from CV through Randles-Sevcik (Eq. (7)) to calculate the peak current (i_p) using scan rate (ν) in an observed voltammogram. For redox reaction cycles, peak current (i_p) depends on the concentration C, the diffusion coefficient (D), the scan rate (ν), and the electrode surface area (A) of redox-active species. [96,97]

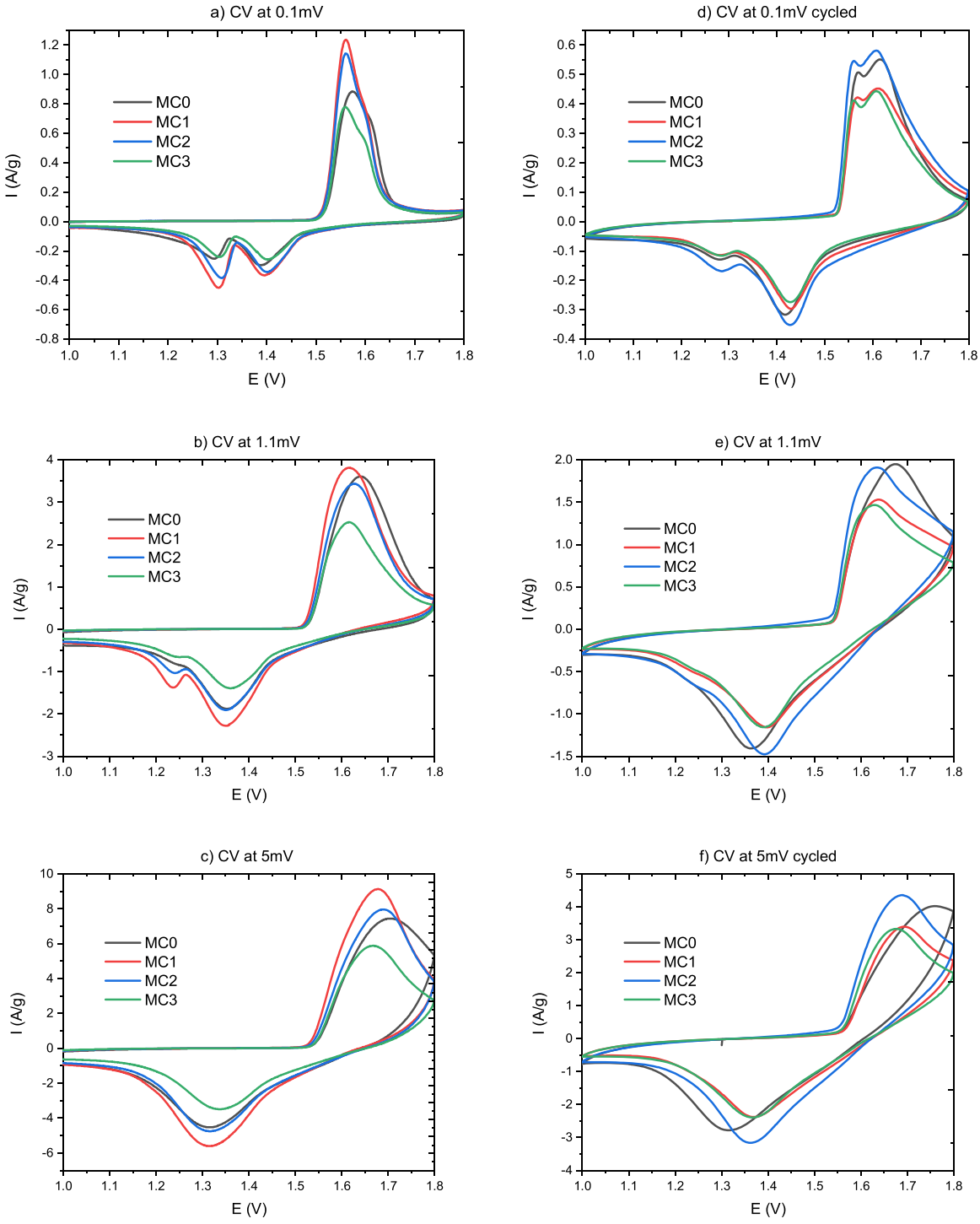

Fig. 4. CV test of the coin cells before and after cycling: a) at 0.1 mV·S^{-1}; b) at 1.1 mV·S^{-1}; a) at 5 mV·S^{-1} a) at 0.1 mV·S^{-1} after cycling; a) at 1.1 mV·S^{-1} after cycling; a) at 5 mV·S^{-1}after cycling.

$$i_p = 0.4463\left(\frac{n^3FF^3}{RT}\right)^{1/2} A \bullet C \bullet (D \bullet v)^{1/2} \quad (7)$$

Where i_p is the Peak current (amperes), n is the Number of electrons transferred in a redox cycle, F is Faraday's constant (96485 C·mol^{-1}), R is the Universal gas constant (8.3145 J·K^{-1} ·mol^{-1}), T is Absolute temperature, A is the electrode surface area in working (cm^2), C is the Molar concentration of redox-active species (mol·cm^{-3}), D is the diffusion coefficient (cm^2 s^{-1}), ν is the scan rate in V·s^{-1}. The calculated diffusion efficiencies (D) are in good agreement with their electrochemical performance in coin cells, with MC1 exhibits the highest D before cycling. The diffusion coefficient data are presented in Fig. 11 together with those data deduced from EIS tests.

3.4. Rate and cycling tests of the zinc-ion batteries

Fig. 7 shows the rate performances of MnO_2 cathodes, at various specific current densities of 20, 50, 100, 200, and 500 mA·g^{-1}. The capacities of MC1 and MC2 are much higher than non-doped MnO_2. At a higher doping level, the electrochemical performance of MC3 is lower

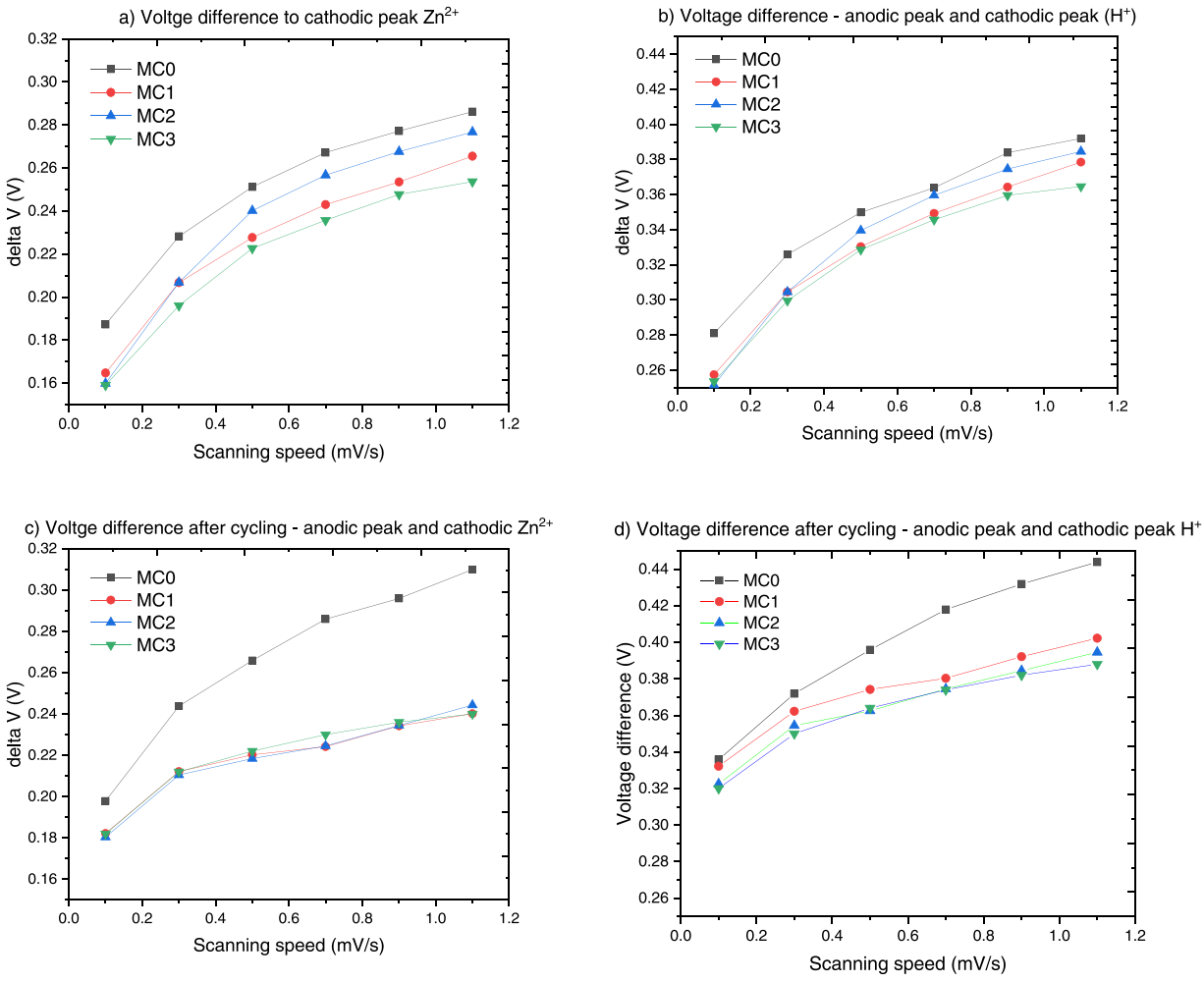

Fig. 5. Redox peak potential difference from CV tests of the coin cells before and after cycling: a) the potential difference between anodic peak and the cathodic peak of Zn^{2+}; b) the potential difference between anodic peak and the cathodic peak of H^{+}; c) the potential difference after cycling between anodic peak and the cathodic peak of Zn^{2+}; d) the potential difference between anodic peak and the cathodic peak of H^{+}.

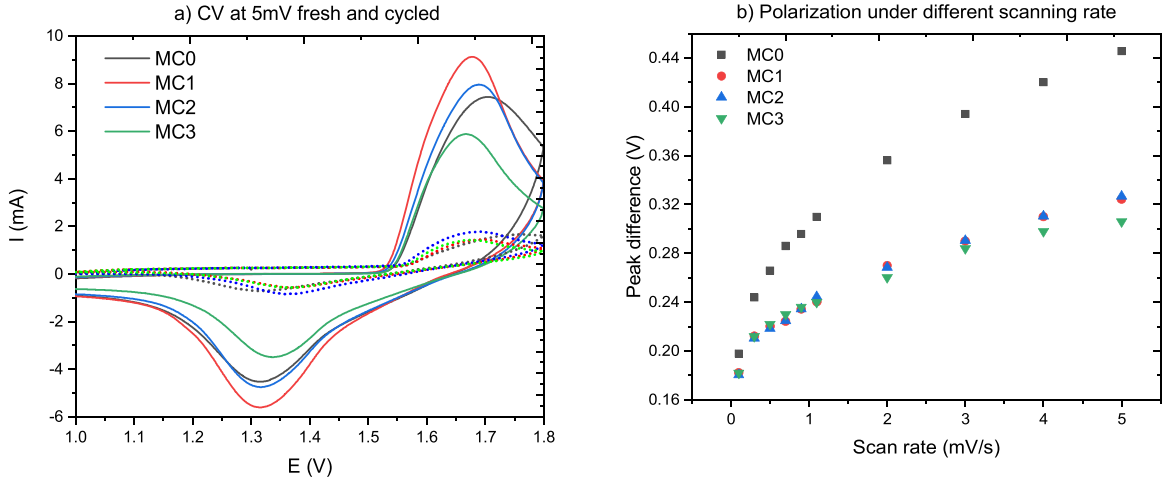

Fig. 6. a) CV tests of the coin cells at 5 mV rate before and after cycling; b) Redox peaks potential difference of the coin cells after cycling, under varied scan rate of 1 ~ 5 mV/s.

than the non-doped MnO_2 sample. When cycled at a specific current density of 200 mA·g^{-1}, MC2 delivered a discharge capacity of 276 and charge capacity of 298 mAh·g^{-1}. The rate capability and capacity are satisfactory when compared to other reports [69,72,74].

The cycling tests are carried out at 200 mA·g^{-1}. The columbic efficiencies are around 99%. MC2 performed the best among all the samples. The capacity retention is 76.7% for MC0. MC1 experienced fast fading with a poor capacity retention of 56.8% after 100 cycles. It was

Table 2
The slope of the linear fitting of lni versus lnν, from the CV tests on coin cells.

		MC0	MC1	MC2	MC3
Fresh cells	b_o	0.589	0.466	0.459	0.491
	$b^{2+}_{r\text{-}Zn}$	0.771	0.768	0.718	0.705
	$b^{+}_{r\text{-}H}$	0.505	0.468	0.416	0.425
Cycled cells	b_o	0.523	0.502	0.491	0.494
	$b^{2+}_{r\text{-}Zn}$	0.620	0.565	0.594	0.597
	$b^{+}_{r\text{-}H}$	0.647	0.612	0.562	0.590

85.8% for MC2 and 74.7% for MC3. This behaviour indicates that the Cu doped MnO_2 are promising candidates for the Zn^{2+} ion storage material. This suggests that optimized level of Cu doping could improve both the cycling and rate performance as well as the stability for ZIBs. The cyclability is not ideal, which could be related to their needle-like morphology and nanoscale particle size as shown in Fig. 1. Further investigation on Cu doped MnO_2 with different particle morphology could be helpful.

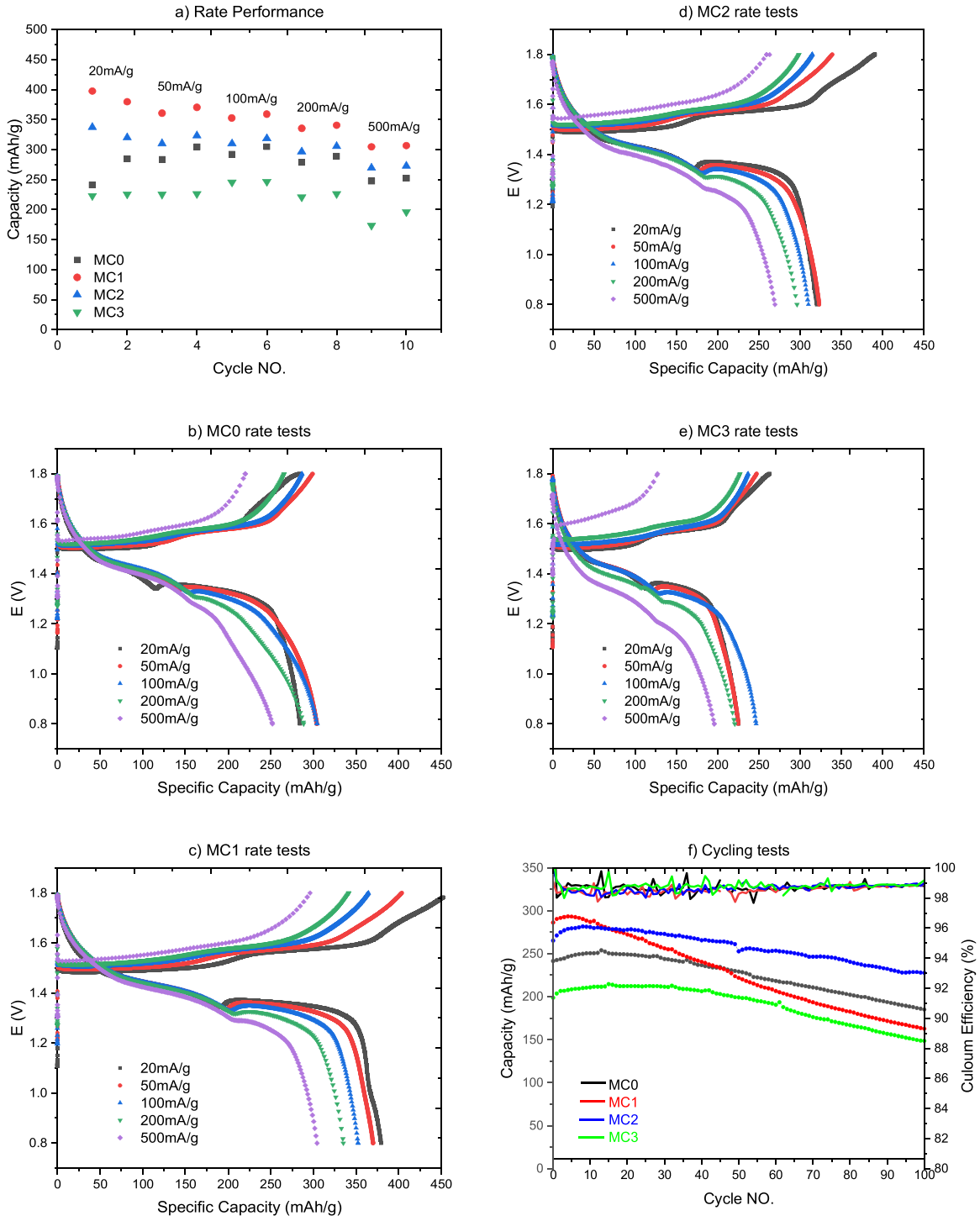

Fig. 7. The rate and cycling performances of full zinc-ion coin cells using different MnO_2 cathodes (non-doped and different level of copper doping): a) initial rate performance; b) rate tests of MC0; c) rate tests of MC1; d) rate tests of MC2; e) rate tests of MC3; f) cycling tests.

3.5. EIS tests of the zinc-ion batteries before and after cycling

Fig. 8 displaces EIS results. The curves consist of depressed semi-circles and diffusion drift which can be fitted using the equivalent circuit as shown in Fig. 9, where Rs, Ri, Rct, CPE, and Zw represent series resistance, interfacial resistance between the electrolyte and electrode, charge transfer resistance, constant phase element, and Warburg diffusion process, respectively.

The Rct value from EIS fitting are shown in Table 2. MC1 showed the lowest Rct before cycling, and MC2 gave the lowest Rct after cycling, which is in good agreement with the electrochemical performance before and after cycling. It is noted that, the charge transfer resistances are high, which agrees with the low diffusion coefficients as calculated, which is also believed to be the main reason of the not very satisfying cycling performance in this research. It can be solved by improving the electrical conductivity of the samples through constructing a conductive support using the graphite, while preparing the cathode active materials. If as synthesized α-MnO_2 are dispersed on graphite, it will increase the contact area between the electrode and the electrolyte and provides more electrochemically active sites for ion-insertion, which can hopefully also enable higher rate performance.

The relationship between real impedance (Z′) and angular frequency (ω) in the low frequency region can be expressed accordingly as follows [97]:

$$Z' = Rs + Ri + Rct + \sigma\omega^{-1/2} \quad (8)$$

σ is the Warburg factor which is relative to Z′- $\omega^{-1/2}$ obtained from the slope of the lines as shown in Fig. 10.

The diffusion coefficient of zinc ion can be calculated as in the following equation [98–101]:

$$D = R^2T^2/2A^2n^4F^4C^2\sigma^2 \quad (5)$$

R is the gas constant, T is the absolute temperature, n is the number of electrons per molecule oxidized (2 for Zinc ions), A is the surface area, F is Faraday's constant, C is the concentration and D is the diffusion coefficient.

The calculated diffusion coefficients of Zinc ions from EIs are in good agreement with the results from CV tests, although slightly lower, due to the testing technique. The diffusion coefficient of samples with higher copper doping - MC2 and MC3 both increased after cycling. Among them MC1 showed highest diffusion before cycling, which is consistent with the cell performance at the beginning of cycling tests. After cycling MC2 gives the highest diffusion coefficient which also matches the results from cycling tests.

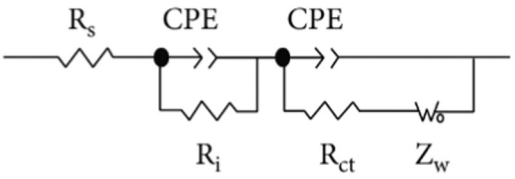

Fig. 9. Equivalent circuit.

Table 3
Rct value from EIS fitting.

	MC0	MC1	MC2	MC3
Rs (Ω)-Fresh	1.742	1.976	2.646	7.39
Rs (Ω)-Cycled	6.637	1.172	2.392	1.779
Ri (Ω)-Fresh	0.699	0.803	0.946	1.118
Ri (Ω)-Cycled	1.921	3.252	1.342	1.305
Rct (Ω)-Fresh	344.5	267.2	359.6	526.5
Rct (Ω)-Cycled	871.6	782.6	529.1	812.6

4. Conclusions

Homogenous Copper-doped Manganese Dioxide has been synthesised and investigated as cathode materials for ZIBs with different doping levels. All the Cu doped MnO_2 are found to be single phase α-MnO_2. Their electrochemical properties as cathode for Zinc-ion batteries are studied. Their pseudo-capacitive behaviour has been investigated, which reveals that charging/discharging processes after cycling are diffusion controlled, while the discharging in fresh cells is a combined process with both capacitive and diffusion contributions. MC2 is found to be the optimum doping level, gives improved performance and better stability, when compared to non-doped MnO_2 samples. MC1 has shown the highest initial capacity of 379.5 mAh·g^{-1} at 0.02 mAh·g^{-1} rate, but it experienced fast fading with a capacity retention of 56.8% after 100 cycles. MC3 showed the lowest capacity among all the samples, suggesting higher level of does not give more benefits. The MC samples showed satisfactory electrochemical properties such as higher capacity and better rate capability, while the non-ideal cyclability could be related to their needle-like morphology and nanoscale particle size. The zinc ion diffusion coefficient of all samples before and after cycling are tested to be in the range of 10^{-12} cm·s^{-1} with a good consistency with their according cell performances, using both cyclic voltammetry and electrochemical impedance spectroscopy. The redox peak difference has been notably reduced, at a similar level for all copper doped samples, compared to non-doped MnO_2. It was noticed that the cell

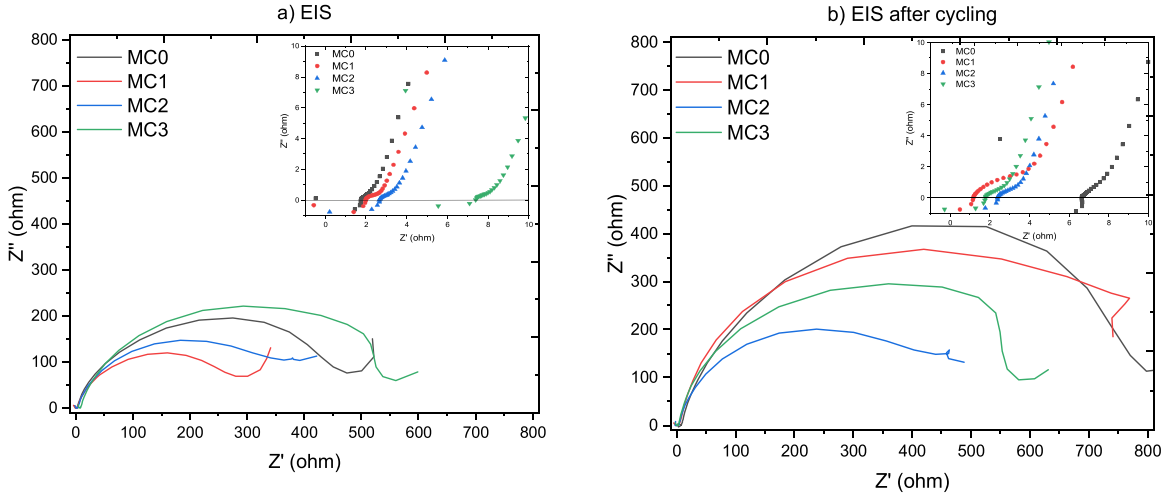

Fig. 8. EIS test of the coin cells a) before and b) after cycling.

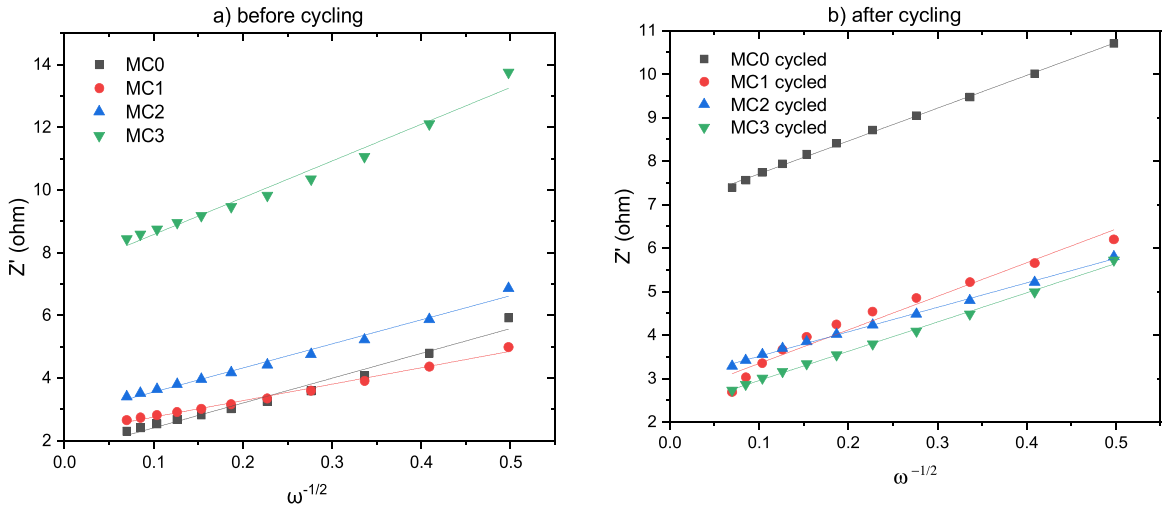

Fig. 10. Warburg factor from Z′- $\omega^{-1/2}$ plot: a) cells before cycling; b) cells after cycling.

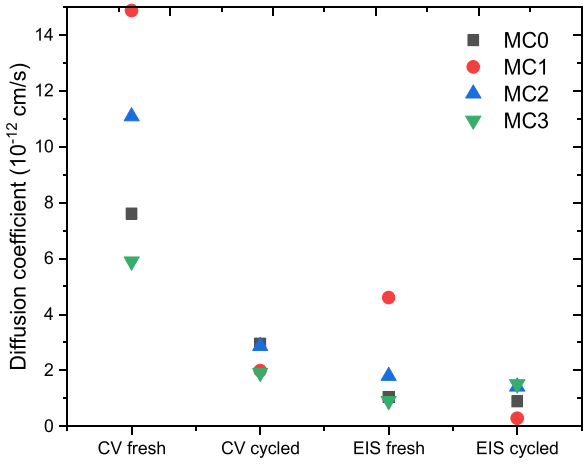

Fig. 11. Diffusion coefficients from CV and EIS tests before and after cycling.

Table 4
Diffusion coefficient from EIS tests.

Diffusion coefficient (10^{-12} $cm^2 \cdot S^{-1}$)	MC0	MC1	MC2	MC3
D fresh	2.202	5.024	2.342	1.006
D cycled	2.429	2.318	4.353	3.057

resistance of non-doped MnO_2 increased from 1.78 Ω to 7.39 Ω, while the cell resistance of Cu-doped cathode all experienced slight reduction during cycling. The results from this paper suggested that Cu-doping is effective to reduce the polarization during charge-discharge, to reduce the resistance, and improve the cycling stability of MnO_2. In this report, the doping level of copper in MnO_2 from hydrothermal process is significantly lower than that in the prepared precursor. Further effort is required to investigate copper doping at higher levels for further investigation. Suitable supporting conductive materials with implementation of nanomaterials such as carbon nanotubes or graphene, could be helpful to improve the Zn^{2+} diffusion. New processes of materials synthesis, supporting conductive materials or second doping could be considered to improve the capacitive behaviour of the cathode materials.

CRediT authorship contribution statement

Alexander Roberts: Writing – review & editing. **Rohit Bhagat:** Resources, Funding acquisition. **Agata Greszta:** Investigation. **Ali Jawad Sahib Sahib:** Investigation. **Evangelos Gkanas:** Writing – review & editing, Supervision. **Rong Lan:** Writing – review & editing, Writing – original draft, Supervision, Methodology, Investigation, Conceptualization.

Declaration of Competing Interest

The authors declare that they have no known competing financial interests or personal relationships that could have appeared to influence the work reported in this paper.

Data Availability

Data will be made available on request.

Acknowledgements

This work was supported by the Trailblazer PhD studentship project, funded by Coventry University.

Appendix A. Supporting information

Supplementary data associated with this article can be found in the online version at doi:10.1016/j.jallcom.2024.174528.

References

[1] X. Wu, X. Ji, Aqueous batteries get energetic, Nat. Chem. 11 (2019) 680–681.
[2] D. Chao, W. Zhou, F. Xie, C. Ye, H. Li, M. Jaroniec, S.-Z. Qiao, Roadmap for advanced aqueous batteries: From design of materials to applications, Sci. Adv. 6 (2020) eaba4098.
[3] Y. Liang, Y. Yao, Designing modern aqueous batteries, Nat. Rev. Mater. 8 (2023) 109–122.
[4] B. Tang, L. Shan, S. Liang, J. Zhou, Issues and opportunities facing aqueous zinc-ion batteries, Energy Environ. Sci. 12 (2019) 3288–3304.
[5] G. Fang, J. Zhou, A. Pan, S. Liang, Recent advances in aqueous zinc-ion batteries, ACS Energy Lett. 3 (2018) 2480–2501.
[6] X. Jia, C. Liu, Z.G. Neale, J. Yang, G. Cao, Active materials for aqueous zinc ion batteries: synthesis, crystal structure, morphology, and electrochemistry, Chem. Rev. 120 (2020) 7795–7866.
[7] B. Yong, D. Ma, Y. Wang, H. Mi, C. He, P. Zhang, Understanding the design principles of advanced aqueous zinc-ion battery cathodes: from transport kinetics to structural engineering, and future perspectives, Adv. Energy Mater. 10 (2020) 2002354.

[8] J. Shin, J. Lee, Y. Park, J.W. Choi, Aqueous zinc ion batteries: focus on zinc metal anodes, Chem. Sci. 11 (2020) 2028–2044.
[9] W. Du, E.H. Ang, Y. Yang, Y. Zhang, M. Ye, C.C. Li, Challenges in the material and structural design of zinc anode towards high-performance aqueous zinc-ion batteries, Energy Environ. Sci. 13 (2020) 3330–3360.
[10] J. Yang, B. Yin, Y. Sun, H. Pan, W. Sun, B. Jia, S. Zhang, T. Ma, Zinc anode for mild aqueous zinc-ion batteries: challenges, strategies, and perspectives, Nano-Micro Lett. 14 (2022) 1–47.
[11] J. Ding, Z. Du, B. Li, L. Wang, S. Wang, Y. Gong, S. Yang, Unlocking the potential of disordered rocksalts for aqueous zinc-ion batteries, Adv. Mater. 31 (2019) 1904369.
[12] X. Wang, Z. Zhang, B. Xi, W. Chen, Y. Jia, J. Feng, S. Xiong, Advances and perspectives of cathode storage chemistry in aqueous zinc-ion batteries, ACS Nano 15 (2021) 9244–9272.
[13] X. Li, Z. Chen, Y. Yang, S. Liang, B. Lu, J. Zhou, The phosphate cathodes for aqueous zinc-ion batteries, Inorg. Chem. Front. 9 (2022) 3986–3998.
[14] Y. Li, J. Zhao, Q. Hu, T. Hao, H. Cao, X. Huang, Y. Liu, Y. Zhang, D. Lin, Y. Tang, Prussian blue analogs cathodes for aqueous zinc ion batteries, Mater. Today Energy (2022) 101095.
[15] T. Zhou, L. Zhu, L. Xie, Q. Han, X. Yang, L. Chen, G. Wang, X. Cao, Cathode materials for aqueous zinc-ion batteries: a mini review, J. Colloid Interface Sci. 605 (2022) 828–850.
[16] S. Huang, J. Zhu, J. Tian, Z. Niu, Recent progress in the electrolytes of aqueous zinc-ion batteries, Chem. –A Eur. J. 25 (2019) 14480–14494.
[17] S. Guo, L. Qin, T. Zhang, M. Zhou, J. Zhou, G. Fang, S. Liang, Fundamentals and perspectives of electrolyte additives for aqueous zinc-ion batteries, Energy Storage Mater. 34 (2021) 545–562.
[18] H. Yan, X. Zhang, Z. Yang, M. Xia, C. Xu, Y. Liu, H. Yu, L. Zhang, J. Shu, Insight into the electrolyte strategies for aqueous zinc ion batteries, Coord. Chem. Rev. 452 (2022) 214297.
[19] Y. Zhu, J. Yin, X. Zheng, A.-H. Emwas, Y. Lei, O.F. Mohammed, Y. Cui, H. N. Alshareef, Concentrated dual-cation electrolyte strategy for aqueous zinc-ion batteries, Energy Environ. Sci. 14 (2021) 4463–4473.
[20] Y. Geng, L. Pan, Z. Peng, Z. Sun, H. Lin, C. Mao, L. Wang, L. Dai, H. Liu, K. Pan, Electrolyte additive engineering for aqueous Zn ion batteries, Energy Storage Mater. 51 (2022) 733–755.
[21] L. Yuan, J. Hao, C.-C. Kao, C. Wu, H.-K. Liu, S.-X. Dou, S.-Z. Qiao, Regulation methods for the Zn/electrolyte interphase and the effectiveness evaluation in aqueous Zn-ion batteries, Energy Environ. Sci. 14 (2021) 5669–5689.
[22] Y. Li, Z. Wang, Y. Cai, M.E. Pam, Y. Yang, D. Zhang, Y. Wang, S. Huang, Designing advanced aqueous zinc-ion batteries: principles, Strateg., Perspect. Energy Environ. Mater. 5 (2022) 823–851.
[23] Q. Zhang, J. Luan, Y. Tang, X. Ji, H. Wang, Interfacial design of dendrite-free zinc anodes for aqueous zinc-ion batteries, Angew. Chem. Int. Ed. 59 (2020) 13180–13191.
[24] X. Gao, H. Wu, W. Li, Y. Tian, Y. Zhang, H. Wu, L. Yang, G. Zou, H. Hou, X. Ji, H +-insertion boosted α-MnO2 for an aqueous Zn-ion battery, Small 16 (2020) 1905842.
[25] J. Zhang, W. Li, J. Wang, X. Pu, G. Zhang, S. Wang, N. Wang, X. Li, Engineering p-band center of oxygen boosting H+ intercalation in δ-MnO2 for aqueous zinc ion batteries, Angew. Chem. Int. Ed. 62 (2023) e202215654.
[26] Y. Liao, H.-C. Chen, C. Yang, R. Liu, Z. Peng, H. Cao, K. Wang, Unveiling performance evolution mechanisms of MnO2 polymorphs for durable aqueous zinc-ion batteries, Energy Storage Mater. 44 (2022) 508–516.
[27] Y. Zhao, Y. Zhu, X. Zhang, Challenges and perspectives for manganese-based oxides for advanced aqueous zinc-ion batteries, InfoMat 2 (2020) 237–260.
[28] G. Li, H. Liang, H. Ren, L. Zhou, M. Hashem, Enhanced high-performance aqueous zinc ion batteries with copper-doped α-MnO2 nanosheets cathodes, J. Nanoelectron. Optoelectron. 18 (2023) 931–937.
[29] Y. Shang, D. Kundu, A path forward for the translational development of aqueous zinc-ion batteries, Joule 7 (2023) 244–250.
[30] S.H. Kim, S.M. Oh, Degradation mechanism of layered MnO2 cathodes in Zn/ZnSO4/MnO2 rechargeable cells, J. Power Sources 72 (1998) 150–158.
[31] M. Zhou, Y. Chen, G. Fang, S. Liang, Electrolyte/electrode interfacial electrochemical behaviors and optimization strategies in aqueous zinc-ion batteries, Energy Storage Mater. 45 (2022) 618–646.
[32] H. Luo, L. Wang, P. Ren, J. Jian, X. Liu, C. Niu, D. Chao, Atomic engineering promoted electrooxidation kinetics of manganese-based cathode for stable aqueous zinc-ion batteries, Nano Res. 15 (2022) 8603–8612.
[33] H. Tang, W. Chen, N. Li, Z. Hu, L. Xiao, Y. Xie, L. Xi, L. Ni, Y. Zhu, Layered MnO2 nanodots as high-rate and stable cathode materials for aqueous zinc-ion storage, Energy Storage Mater. 48 (2022) 335–343.
[34] X. Shen, X. Wang, N. Yu, W. Yang, Y. Zhou, Y. Shi, Y. Wang, L. Dong, J. Di, Q.L.A. P.-C. MnO, 2/Carbon nanotube film cathode for rechargeable aqueous Zn-ion batteries, Acta Phys. -Chim. Sin. 38 (2022), 2006059-2006050.
[35] T. Zhang, Y. Tang, S. Guo, X. Cao, A. Pan, G. Fang, J. Zhou, S. Liang, Fundamentals and perspectives in developing zinc-ion battery electrolytes: a comprehensive review, Energy Environ. Sci. 13 (2020) 4625–4665.
[36] P. Ruan, S. Liang, B. Lu, H.J. Fan, J. Zhou, Design strategies for high-energy-density aqueous zinc batteries, Angew. Chem. 134 (2022) e202200598.
[37] F. Gao, W. Shi, B. Jiang, Z. Xia, L. Zhang, Q. An, Ni/Fe bimetallic ions co-doped manganese dioxide cathode materials for aqueous zinc-ion batteries, Batteries 9 (2023) 50.
[38] H. Li, Z. Huang, B. Chen, Y. Jiang, C. Li, W. Xiao, X. Yan, A high-performance MnO2 cathode doped with group VIII metal for aqueous Zn-ion batteries: In-situ X-ray diffraction study on Zn2+ storage mechanism, J. Power Sources 527 (2022) 231198.
[39] J.-W. Xu, Q.-L. Gao, Y.-M. Xia, X.-S. Lin, W.-L. Liu, M.-M. Ren, F.-G. Kong, S.-J. Wang, C. Lin, High-performance reversible aqueous zinc-ion battery based on iron-doped alpha-manganese dioxide coated by polypyrrole, J. Colloid Interface Sci. 598 (2021) 419–429.
[40] M.A. Kamenskii, F.S. Volkov, S.N. Eliseeva, E.G. Tolstopyatova, V.V. Kondratiev, Enhancement of electrochemical performance of aqueous zinc ion batteries by structural and interfacial design of MnO2 cathodes: the metal ion doping and introduction of conducting polymers, Energies 16 (2023) 3221.
[41] M. Aadil, S. Zulfiqar, M. Shahid, S. Haider, I. Shakir, M.F. Warsi, Binder free mesoporous Ag-doped Co3O4 nanosheets with outstanding cyclic stability and rate capability for advanced supercapacitor applications, J. Alloy. Compd. 844 (2020) 156062.
[42] M. Aadil, G. Nazik, S. Zulfiqar, I. Shakir, M.F.A. Aboud, P.O. Agboola, S. Haider, M.F. Warsi, Fabrication of nickel foam supported Cu-doped Co3O4 nanostructures for electrochemical energy storage applications, Ceram. Int. 47 (2021) 9225–9233.
[43] M. Aadil, A.G. Taki, S. Zulfiqar, A. Rahman, M. Shahid, M.F. Warsi, Z. Ahmad, A. A. Alothman, S. Mohammad, Gadolinium doped zinc ferrite nanoarchitecture reinforced with a carbonaceous matrix: a novel hybrid material for next-generation flexible capacitors, RSC Adv. 13 (2023) 28063–28075.
[44] Y. Zhao, P. Zhang, J. Liang, X. Xia, L. Ren, L. Song, W. Liu, X. Sun, Uncovering sulfur doping effect in MnO2 nanosheets as an efficient cathode for aqueous zinc ion battery, Energy Storage Mater. 47 (2022) 424–433.
[45] S. Kim, B.-R. Koo, Y.-R. Jo, H.-R. An, Y.-G. Lee, C. Huang, G.-H. An, Defect engineering via the F-doping of β-MnO 2 cathode to design hierarchical spheres of interlaced nanosheets for superior high-rate aqueous zinc ion batteries, J. Mater. Chem. A 9 (2021) 17211–17222.
[46] Y. Zhang, Y. Liu, Z. Liu, X. Wu, Y. Wen, H. Chen, X. Ni, G. Liu, J. Huang, S. Peng, MnO2 cathode materials with the improved stability via nitrogen doping for aqueous zinc-ion batteries, J. Energy Chem. 64 (2022) 23–32.
[47] T. Chen, X. Liu, X. Shen, B. Dai, Q. Xu, Improving stability and reversibility of manganese dioxide cathode materials via nitrogen and sulfur doping for aqueous zinc ion batteries, J. Alloy. Compd. 943 (2023) 169068.
[48] Z. Zhang, S. Li, B. Zhao, X. Zhang, X. Wang, Z. Wen, S. Ji, J. Sun, Joint influence of nitrogen doping and oxygen vacancy on manganese dioxide as a high-capacity cathode for zinc-ion batteries, J. Phys. Chem. C. 125 (2021) 20195–20203.
[49] G. Cui, Y. Zeng, J. Wu, Y. Guo, X. Gu, X.W. Lou, Synthesis of nitrogen-doped KMn8O16 with oxygen vacancy for stable zinc-ion batteries, Adv. Sci. 9 (2022) 2106067.
[50] M. Aadil, S. Zulfiqar, P.O. Agboola, M.F.A. Aboud, I. Shakir, M.F. Warsi, Fabrication of graphene supported binary nanohybrid with multiple approaches for electrochemical energy storage applications, Synth. Met. 272 (2021) 116645.
[51] X. Li, Q. Zhou, Z. Yang, X. Zhou, D. Qiu, H. Qiu, X. Huang, Y. Yu, Unraveling the role of nitrogen-doped carbon nanowires incorporated with MnO2 nanosheets as high performance cathode for zinc-ion batteries, Energy Environ. Mater. 6 (2023) e12378.
[52] Z. Wang, M. Zhang, W. Ma, J. Zhu, W. Song, Application of carbon materials in aqueous zinc ion energy storage devices, Small 17 (2021) 2100219.
[53] H. Wang, R. Guo, Y. Ma, F. Zhou, Cross-doped Mn/Mo oxides with core-shell structures designed by a self-template strategy for durable aqueous zinc-ion batteries, Adv. Funct. Mater. (2023) 2301351.
[54] Z. Ni, X. Liang, L. Zhao, H. Zhao, B. Ge, W. Li, Tin doping manganese dioxide cathode materials with the improved stability for aqueous zinc-ion batteries, Mater. Chem. Phys. 287 (2022) 126238.
[55] Y. Zhong, X. Xu, J.-P. Veder, Z. Shao, Self-recovery chemistry and cobalt-catalyzed electrochemical deposition of cathode for boosting performance of aqueous zinc-ion batteries, Iscience 23 (2020) 100943–100957.
[56] Y. Song, J. Li, R. Qiao, X. Dai, W. Jing, J. Song, Y. Chen, S. Guo, J. Sun, Q. Tan, Binder-free flexible zinc-ion batteries: one-step potentiostatic electrodeposition strategy derived Ce doped-MnO2 cathode, Chem. Eng. J. 431 (2022) 133387.
[57] H. Yang, Y. Wan, K. Sun, M. Zhang, C. Wang, Z. He, Q. Li, N. Wang, Y. Zhang, H. Hu, Reconciling mass loading and gravimetric performance of MnO2 cathodes by 3D-printed carbon structures for zinc-ion batteries, Adv. Funct. Mater. (2023) 2215076.
[58] W.Y. Ko, A.L. Lubis, H.Y. Wang, T.C. Wu, S.T. Lin, K.J. Lin, Facile construction of Zn-doped Mn3O4– MnO2 vertical nanosheets for aqueous zinc-ion battery cathodes, ChemElectroChem 9 (2022) e202200750.
[59] L. Bigiani, C. Maccato, A. Gasparotto, C. Sada, E. Bontempi, D. Barreca, Plasma-assisted chemical vapor deposition of F-doped MnO2 nanostructures on single crystal substrates, Nanomaterials 10 (2020) 1335.
[60] Z. Bassyouni, A. Allagui, J.D. Abou Ziki, Microsized electrochemical energy storage devices and their fabrication techniques for portable applications, Adv. Mater. Technol. 8 (2023) 2200459.
[61] A.M. Hashem, H.M. Abuzeid, N. Narayanan, H. Ehrenberg, C. Julien, Synthesis, structure, magnetic, electrical and electrochemical properties of Al, Cu and Mg doped MnO2, Mater. Chem. Phys. 130 (2011) 33–38.
[62] Y. Zhang, Y. Hu, S. Li, J. Sun, B. Hou, Manganese dioxide-coated carbon nanotubes as an improved cathodic catalyst for oxygen reduction in a microbial fuel cell, J. Power Sources 196 (2011) 9284–9289.
[63] X. Li, B. Hu, S. Suib, Y. Lei, B. Li, Manganese dioxide as a new cathode catalyst in microbial fuel cells, J. Power Sources 195 (2010) 2586–2591.
[64] D.J. Davis, T.N. Lambert, J.A. Vigil, M.A. Rodriguez, M.T. Brumbach, E.N. Coker, S.J. Limmer, Role of Cu-ion doping in Cu-α-MnO2 nanowire electrocatalysts for the oxygen reduction reaction, J. Phys. Chem. C. 118 (2014) 17342–17350.

[65] B. Jiang, T. Muddemann, U. Kunz, H. Bormann, M. Niedermeiser, D. Haupt, O. Schläfer, M. Sievers, Evaluation of microbial fuel cells with graphite plus MnO2 and MoS2 paints as oxygen reduction cathode catalyst, J. Electrochem. Soc. 164 (2016) H3083.
[66] S. Xu, L. Lu, L. Liu, Z. Luo, S. Wang, G. Li, C. Feng, Hydrothermal synthesis of Cu-doped β-MnO2 nanorods as cathode material for lithium ion battery applications, J. Nanosci. Nanotechnol. 17 (2017) 2109–2115.
[67] L. He, J. Wu, D. Lau, C. Hall, Y. Jiang, B. Thapa, Y. Gao, T. Yeung, A. Wotton, A. Lennon, Combined Ag and Cu-doping of MnO2-x improves Li-ion battery capacity retention on cycling, Mater. Lett. 304 (2021) 130659.
[68] N. Kumagai, S. Komaba, K. Abe, H. Yashiro, Synthesis of metal-doped todorokite-type MnO2 and its cathode characteristics for rechargeable lithium batteries, J. Power Sources 146 (2005) 310–314.
[69] T.-H. Wu, W.-Y. Liang, Y.-Q. Lin, Facile synthesis of Cu− intercalated MnO2 nanoflakes cathode for enhanced energy storage in zinc− ion batteries, J. Taiwan Inst. Chem. Eng. 131 (2022) 104172.
[70] Z. Raheem, A. Al Sammarraie, Synthesis of different manganese dioxide nanostructures and studding the enhancement of their electrochemical behavior in zinc–Mno2 rechargeable batteries by doping with copper. AIP Conference Proceedings, AIP Publishing, 2020.
[71] G.G. Yadav, J.W. Gallaway, D.E. Turney, M. Nyce, J. Huang, X. Wei, S. Banerjee, Regenerable Cu-intercalated MnO2 layered cathode for highly cyclable energy dense batteries, Nat. Commun. 8 (2017) 14424.
[72] Y. Chen, S. Gu, S. Wu, X. Ma, I. Hussain, Z. Sun, Z. Lu, K. Zhang, Copper activated near-full two-electron Mn4+/Mn2+ redox for mild aqueous Zn/MnO2 battery, Chem. Eng. J. 450 (2022) 137923.
[73] L. Ren, G. Yu, H. Xu, W. Wang, Y. Jiang, M. Ji, S. Li, Doping-induced static activation of MnO2 cathodes for aqueous Zn-ion batteries, ACS Sustain. Chem. Eng. 9 (2021) 12223–12232.
[74] S.-M. Ma, T.-X. Wang, Z.-Y. Deng, X.-S. Zheng, B.-B. Wang, H.-J. Feng, Improved performance of Cu ion implanted δ-MnO2 cathode material for aqueous Zn-ion batteries, Phys. Lett. A 451 (2022) 128400.
[75] D. Mondal, S. Das, B.K. Paul, D. Bhattacharya, D. Ghoshal, A.L. Gayen, K. Das, S. Das, Size engineered Cu-doped α-MnO2 nanoparticles for exaggerated photocatalytic activity and energy storage application, Mater. Res. Bull. 115 (2019) 159–169.
[76] M.U. Khalid, M. Al Huwayz, S. Zulfiqar, E.W. Cochran, Z. Alrowaili, M. Al-Buriahi, M.F. Warsi, M. Shahid, Phase transformation of α-MnO2 to β-MnO2 induced by Cu doping: improved electrochemical performance for next generation supercapacitor, Mater. Sci. Eng.: B 295 (2023) 116580.
[77] S. Jangu, S. Kumar, K.N. Deepika, C. Jacob, D. Pradhan, Effect of microwave power and Cu doping on MnO2 nanostructures and its supercapacitor performance, ACS Appl. Electron. Mater. 5 (2023) 3078–3092.
[78] B. Aljafari, S. James, J.J. Wu, S. Anandan, Synthesized sea urchin morphology of copper incorporated hollandite manganese dioxide for energy storage applications, J. Alloy. Compd. (2023) 171036.
[79] J. Wang, J. Fan, J. Yao, X. Wu, C. Gao, Z. Wei, Y. Li, Facet tailoring and Cu doping promoted photo-assisted peroxymonosulfate activation by oxygen-deficient α-MnO2 for efficient mineralization of Bisphenol A, Chem. Eng. J. 461 (2023) 142024.
[80] Y. Yang, Y. Li, M. Zeng, M. Mao, L. Lan, H. Liu, J. Chen, X. Zhao, UV–vis-infrared light-driven photothermocatalytic abatement of CO on Cu doped ramsdellite MnO2 nanosheets enhanced by a photoactivation effect, Appl. Catal. B: Environ. 224 (2018) 751–760.
[81] J. Gao, C. Jia, L. Zhang, H. Wang, Y. Yang, S.-F. Hung, Y.-Y. Hsu, B. Liu, Tuning chemical bonding of MnO2 through transition-metal doping for enhanced CO oxidation, J. Catal. 341 (2016) 82–90.
[82] Z. Ye, J.-M. Giraudon, N. Nuns, G. Abdallah, A. Addad, R. Morent, N. De Geyter, J.-F. Lamonier, Preferential dissolution of copper from Cu-Mn oxides in strong acid medium: Effect of the starting binary oxide to get new efficient copper doped MnO2 catalysts in toluene oxidation, Appl. Surf. Sci. 537 (2021) 147993.
[83] M.T. Nguyen Dinh, C.C. Nguyen, N.H. Thi Phan, H.D. Nguyen Phuc, Q. Van Le, S. Y. Kim, L. Nguyen-Dinh, Tailoring oxygen vacancies and active surface oxygen species in copper-doped MnO2 catalysts for total catalytic oxidation of VOCs, Ind. Eng. Chem. Res. 62 (2023) 6908–6919.
[84] C. Dong, PowderX: Windows-95-based program for powder X-ray diffraction data processing, J. Appl. Crystallogr. 32 (1999), 838-838.
[85] B.H. Toby, R.B. Von Dreele, GSAS-II: the genesis of a modern open-source all purpose crystallography software package, J. Appl. Crystallogr. 46 (2013) 544–549.
[86] T. Li, M. Aadil, S. Zulfiqar, A. Anwar, S.M. Yakout, N.M. Panduro-Tenazoa, S. Mubeen, Synthesis of doped and porous CuO with boosted light-harvesting features for the photocatalytic mineralization of azo dyes, Ceram. Int. 49 (2023) 27827–27836.
[87] P. Scherrer, Bestimmung der Grosse und inneren Struktur von Kolloidteilchen mittels Rontgenstrahlen, Nach Ges. Wiss. Gottingen 2 (1918) 8–100.
[88] W. Wazir, Z. Ahmad, S. Zulfiqar, E.W. Cochran, S. Mubarik, T. Kousar, H. Somaily, J.-J. Shim, H.A. Alsalmah, M. Aadil, Synergistic effects of noble metal doping and nanoengineering on boosting the azo dye mineralization activity of nickel oxide, Ceram. Int. 49 (2023) 38026–38035.
[89] M. Siddiq, A.G. Taki, M. Aadil, S. Mubarik, E.W. Cochran, S. Zulfiqar, A. A. Mohammed, S. Ijaz, Microwave-assisted synthesis of tentacles like Ag-doped copper oxide nano-ceramics: structural, optical, and anti-campylobacter studies, Ceram. Int. 49 (2023) 36590–36599.
[90] G. Nazik, M. Aadil, S. Zulfiqar, W. Hassan, A. Rahman, S.M. Ibrahim, K. Naseem, T.A. Sheikh, M.N. Akhtar, Synthesis of doped metal sulfide nanoparticles and their graphene reinforced nanohybrid for Pb (II) detection, Z. F. üR. Phys. Chem. 237 (2023) 1257–1285.
[91] S. Ayuob, M. Mahmood, N. Ahmad, A. Waqas, H. Saeed, M.B. Sajid, Development and validation of Nusselt number correlations for a helical coil based energy storage integrated with solar water heating system, J. Energy Storage 55 (2022) 105777.
[92] A. Farooq, M. Anwar, H. Somaily, S. Zulfiqar, M.F. Warsi, M.I. Din, A. Muhammad, A. Irshad, Fabrication of Ag-doped magnesium aluminate/rGO composite: a highly efficient photocatalyst for visible light-driven photodegradation of crystal violet and phenol, Phys. B: Condens. Matter 650 (2023) 414508.
[93] S. Khamsanga, R. Pornprasertsuk, T. Yonezawa, A.A. Mohamad, S. Kheawhom, δ-MnO2 nanoflower/graphite cathode for rechargeable aqueous zinc ion batteries, Sci. Rep. 9 (2019) 8441.
[94] Y. De Luna, A. Alsulaiti, M.I. Ahmad, H. Nimir, N. Bensalah, Electrochemically stable tunnel-type α-MnO2-based cathode materials for rechargeable aqueous zinc-ion batteries, Front. Chem. 11 (2023) 1101459.
[95] D. Chen, D. Ding, X. Li, G.H. Waller, X. Xiong, M.A. El-Sayed, M. Liu, Probing the charge storage mechanism of a pseudocapacitive MnO2 electrode using in operando Raman spectroscopy, Chem. Mater. 27 (2015) 6608–6619.
[96] J.J. Van Benschoten, J.Y. Lewis, W.R. Heineman, D.A. Roston, P.T. Kissinger, Cyclic voltammetry experiment, J. Chem. Educ. 60 (1983) 772.
[97] K. Tang, X. Yu, J. Sun, H. Li, X. Huang, Kinetic analysis on LiFePO4 thin films by CV, GITT, and EIS, Electrochim. Acta 56 (2011) 4869–4875.
[98] S. Tang, M. Lai, L. Lu, Study on Li+-ion diffusion in nano-crystalline LiMn2O4 thin film cathode grown by pulsed laser deposition using CV, EIS and PITT techniques, Mater. Chem. Phys. 111 (2008) 149–153.
[99] M. Mahmood, S. Zulfiqar, M.F. Warsi, M. Aadil, I. Shakir, S. Haider, P.O. Agboola, M. Shahid, Nanostructured V2O5 and its nanohybrid with MXene as an efficient electrode material for electrochemical capacitor applications, Ceram. Int. 48 (2022) 2345–2354.
[100] S. Jabeen, M. Aadil, J. Williams, M. Awan, J. Iqbal, S. Zulfiqar, N. Nazar, Synthesis of In2O3/GNPs nanocomposites with integrated approaches to tune overall performance of electrochemical devices, Ceram. Int. 47 (2021) 22345–22355.
[101] M.U. Khalid, K.M. Katubi, S. Zulfiqar, Z. Alrowaili, M. Aadil, M. Al-Buriahi, M. Shahid, M.F. Warsi, Boosting the electrochemical activities of MnO2 for next-generation supercapacitor application: adaptation of multiple approaches, Fuel 343 (2023) 127946.